

# Authors response to reviewer's and editor's comments on GMD 2018-260 "The Matsuno baroclinic wave test case" by Shamir, Yacoby, Ziskin and Paldor

immediate

**Correspondence:** Nathan Paldor (nathan.paldor@huji.ac.il)

## General response

We appreciate the reviewer's meticulous evaluation of both the text and the code. We provide a detailed response to each of his/her comments below. Save for a couple of graphical errors that resulted in the opposite colors between Figs. 1,2 and Fig. 4,5 and the revision of the convergence test, all other comments were found to be only minor comments, which were fully implemented in the revised version. In particular, the potential bug flagged by the reviewer resulted from a misunderstanding and required only clarification in the text.

In order to address the editor's technical comments we have recruited the help of an expert on this issue, who was responsible for packaging the code, verifying (i.e. unit testing), interfacing, licensing and archiving. Consequently, this expert was added as a co-author in acknowledgement of his significant contribution. Please see our detailed response below, following our detailed response to the reviewer's comments.

## Response to the specific comments made by the reviewer

1) Page 3, Eq. (1): Add the definition of the imaginary unit  $i$ .

[Added - see paragraph following Eq. \(1\) of the revised manuscript](#)

In addition, the manuscript (Eq. (1)) fails to state that only the real parts of Eq. (1) and also Eq. (3) are used for the initialization of  $u, v, \Phi, \omega_{n,k,j}$  as coded in the initialization codes.

[Added - see Eqs. \(1\) and \(3\) of the revised manuscript](#)

2) Page 3, line 19: The manuscript omits the definitions of the physical constants  $\omega, a$  and  $g$ . Please add these to promote completeness and reproducibility, since there are many possibilities to set these constants. I assume that it is paramount that the tested shallow water model also needs to use the same constants. Make the user aware of this.

[We assume that the reviewer means the actual numeric values \(the physical definition were already given\). These values were added as requested - see the definitions following Eq. \(2\) in the revised manuscript. \(We note that since the test is analytic](#)

and not an inter-comparison one if different developers use slightly different values they can still compare their simulations to the analytic results provided they use those value in the analytic expressions as well and  $H$  is chose so as to ensure that  $gH$  is small.)

3) Page 4, Eq. (6) and line 20: The expressions for the symbols  $H_n$  and  $\hat{H}_n$  are missing, and the connection between  $H_n$  (in Eq. (6)) and the normalized  $\hat{H}_n$  (line 20) is unclear. Do you imply  $H_n = \hat{H}_n$  as suggested by the code?

The code does not imply that  $\hat{H}_n = H_n$ . What determines the normalization of the calculated polynomials is the specific three-term recurrence relation (including its initialization). The three-term recurrence relation used in the code corresponds to the normalized Hermite polynomials (normalized in the sense that they are orthonormal). The non-normalized one satisfy a slightly different relation.

In case they are the same why are two different symbols used (maybe typo)?

Yes it is a typo, sorry. there is no need for the non-normalized polynomials  $H_n$  at all, only the normalized ones  $\hat{H}_n$  are used. Corrected - see Eq. (6a) of the revised manuscript.

The manuscript points to the Press et al. (2007) ‘Numerical Recipes’ book for the explanation of the Hermite three-term recurrence relation for  $H_n$ . I think this is a major barrier for the adoption of this test case by others, especially if the publication of the initialization codes is dropped. Taking a look at the initialization codes, the exact definition and normalizations for  $H_n$  used here are short enough so that they should be provided in an Appendix to this manuscript. Please add this information for completeness.

Actually, the three-term recurrence relation is short enough and is included in the main text (and too short for an appendix). Please see the new paragraph following Eq. (6) and the new Eq. (7) of the revised manuscript.

4) Page 4, Eq. (6a): There is a mismatch between the definition of  $\hat{v}_n$  (formerly  $\psi_n$  (Eq. (4)) in the first version of the manuscript) and the Fortran/Matlab/Python initialization codes. In the original Fortran/Matlab/Python initialization codes (e.g. line 158 in the Fortran program)  $\psi_n$  is initialized as

$$(\hat{v}_n =)\psi_n = AH_n \exp \left[ -\frac{1}{2} \epsilon^{1/2} \left( \frac{y}{a} \right)^2 \right] \quad (1)$$

but the manuscript defines this quantity as (see the definition of  $\hat{v}_n$  in Eq. (6a)):

$$\hat{v}_n = \psi_n = AH_n \left[ \epsilon^{1/4} \left( \frac{y}{a} \right)^2 \right] \exp \left[ -\frac{1}{2} \epsilon^{1/2} \left( \frac{y}{a} \right)^2 \right] \quad (2)$$

The factor  $\epsilon^{1/4} \left( \frac{y}{a} \right)$  is missing in the codes. Is this a typo in the manuscript or an error in the initialization codes? If it is an error in the initialization codes then all simulations and analyses need to be repeated.

The quantity in square brackets in Eq. (6a) is not a multiplicative factor. It is the argument of the Hermite function  $H_n$  ( $\hat{H}_n$  in the revised version), which was denoted with square brackets instead of the more conventional parentheses due to the use of the latter to encapsulate  $(y/a)$ . In order to simplify the expression we removed the parentheses from  $(y/a)$  and use them for the

function's argument as is more common. We also added a comment in the text that explains it - see note (iii) after Eq. (7) in the revised manuscript. In other word, the independent variable in Eq. (6a) is  $(\epsilon^{1/4}y/a)$ , and not just  $y$ . This is also the way it is coded. The function `get_hermite_polynomial(x,n)` (e.g. lines 116-134 of the Fortran code) is defined for arbitrary independent variable, but when it is called (e.g. in line 158 of the Fortran code) it is called for the independent variable  $(\epsilon^{1/4}y/a)$  (note the definition of  $y$  in line 153).

5) Page 6, line 8: There is a wrong definition of the planar wavenumber  $k$  (with units  $1/m$ ). The parameter  $k$  is confused with its dimensionless spherical counterpart  $ks$ . The definition  $k=5$  needs to read  $ks = 5$  and, for completeness, I recommend also providing the definition of  $k = ks/a$  (for the equatorial plane) again.

Done - third paragraph in Section 3.1 of the revised manuscript

6) Page 6, line 13: When providing the codes, please make sure that the parameters in the codes match the manuscript, e.g. correct the amplitude to  $\text{amp}=10^{-5}$  m/s in the shallow water model (line 117) to match the information for the amplitude  $A$  on page 6, line 13.

Done. The default amplitude is now set to  $e^{-5}$  m/s.

7) Page 8, line 7: The manuscripts fails to describe the boundary conditions (in the  $y$ -direction) for  $u$  and  $\Phi$ . Please add this information for the channel model.

Matsuno's solutions are derived from a second order equation for  $v(y)$  and therefore the **only** boundary conditions required to close the problem are  $v(y) = 0$  at the channel walls. The corresponding values of  $u$  and  $\Phi$  at the channel walls are determined directly from the differential equations themselves.

8) Page 8, lines 31-33, Fig. 2 (g): What does 'appears to be' mean?

We meant that it appears to be  $\pi/4$ , but can be any integer multiple of  $\pi/4$ . In any case we have rephrased the description of Fig. 2 - please see revised discussion of Fig 2. starting on p.9

You seem to suggest that a tiny phase speed error leads to an exact  $\pi/4$  (or any integer multiple of  $\pi/4$  ?) shift of the  $v$  latitude-time diagram (panel g) after 99 wave periods. I find this speculation questionable, and even if true it would not be a tiny error.

We have rephrased the description of Fig. 2 - please see revised discussion of Fig 2. starting on p.9

If there were a phase error like this, why would this not affect all other fields as well? The authors lost me here. Could there be a plotting problem with panels 2g and also 2j (e.g. wrong output file)?

It does affect all other fields. The phase shift between the simulated patterns and the expected ones is the same in all panels (f)-(j) of Figure 2. Note that, while all Hovmoller diagrams are generated at the same longitudinal intersect  $\lambda = -18^\circ$  degrees, this intersect corresponds to a different phase in each of the different initial fields shown in the top row of the figure, as indicated by the vertical white dashed lines. In other words the initial fields themselves have different phases (which is a general property of the SWEs). We originally wrote this discussion for panel (g) thinking that it will simplify the discussion, since  $v$  is independent of the wave type (i.e. it is identical in Rossby and IG modes). Since it ended up being more confusing, we do not single out panel (g) anymore in the revised version - please see revised discussion of Fig 2. starting on p.9

9) Page 10: add a reference for the GFDL spectral transform shallow water model

Unfortunately, this model has no proper reference. We provide a link to its online description on GFDL's website -see first paragraph of Section 4.2.

10) Page 11, line 7: remove double 'the'

Done - thank you

11) Page 11, line 8: remove 'at'

Done - thank you

12) Page 11: Almost all users of the test case will use a global shallow water model, so the addition of the new section 4.2 is very much appreciated. However, the current discussion of the global shallow water results is inadequate and insufficient. In my view, the discussion of the global results is way more important than the discussion of the tropical channel results, but this section seems to be added in a rushed fashion. As mentioned above, I am now stunned to see completely different results for the global shallow water model. Why are the results so different in comparison to the channel model? The authors do not even comment on the fact that e.g. all colors are flipped when comparing the Rossby wave in the tropical channel model (Fig. 1) to the Rossby wave of the global shallow water model (Fig. 4). The same is true for the EIG wave (Figs. 2 and 5). I suspect this is due to an initialization (sign) error in either the channel or the global model. This needs to be investigated, likely reassessed and explained.

The reviewer is right. We expect only little difference between the global model and the equatorial-channel one, provided the channel is sufficiently wide so that the solutions are not affected by the imposed boundary conditions at the walls which are not included in Matsuno's theory. Unfortunately, there were a couple of plotting error that resulted in the opposite signs: 1) The definition of the longitude in the two models is different. The longitude in the equatorial-channel model is defined for  $\lambda_1 \in [-180, 180]$ , whereas the longitude angle in the global model is defined for  $\lambda_2 \in [0, 360]$ . Note that  $\cos(5\lambda_1) = \cos(5(\lambda_2 -$

$\pi)) = -\cos(5\lambda_2)$ . 2) The direction of the latitudes in Fig. 1 and 2 was accidentally (bug-like) flipped. For the chosen parameters initial  $v$  field should increase with latitude at  $\lambda = 0$ .

Despite the unfortunate plotting errors, an opposite sign is hardly a mistake in our view since for linear waves the amplitude is arbitrary so the simulations work just as well with an opposite sign. The only restriction on the amplitude is that it's sufficiently small for the non-linear terms to be negligible, but not too small so as to avoid round-off errors - both of which stem from practical considerations.

Having fixed the graphical errors, the solutions of the global model are indeed similar to those of the equatorial channel. At the risk of being repetitive and in order to respond positively to the reviewer's concerns we repeat some of the explanation from the subsection on the equatorial channel in the spherical model subsection so the two sections can be read independently - please see the revised section 4.2.

13) Figs. 4 and 5 (in comparison to Figs. 1 and 2): I do not see a reason why even the 'initial states' (e.g. comparing hour 0 in Fig. 1 to hour 4 in Fig. 4) show opposite colors. The 4-hour difference in the time snapshots, which I find unnecessary and very irritating, cannot be the reason due to the long wave period of 18.5 days of the Rossby wave. As mentioned in point 12) this looks like a sign error in the initialization to me.

Unfortunately, there were a couple of plotting error that resulted in the opposite signs: 1) The definition of the longitude in the two models is different. The longitude in the equatorial-channel model is defined for  $\lambda_1 \in [-180, 180]$ , whereas the longitude angle in the global model is defined for  $\lambda_2 \in [0, 360]$ . Note that  $\cos(5\lambda_1) = \cos(5(\lambda_2 - \pi)) = -\cos(5\lambda_2)$ . 2) The direction of the latitudes in Fig. 1 and 2 was accidentally (bug-like) flipped. For the chosen parameters initial  $v$  field should increase with latitude at  $\lambda = 0$ .

Change Figs. 4 and 5 and show time step 0 instead of the simulation after 4 hours. In addition, replot Fig. 4 and label the 18W and 18E points (as in all other figures) instead of the 15W and 15E points.

Done - see revised version of the figures

14) Figs. 4 and 5: Figs. 1 and 2 are normalized with the initial states at  $t=0$ . Did you normalize Figs. 4 and 5 with the state after 4 hours or with the state at  $t=0$ ? If the state after 4 hours was used, correct the normalization (use  $t=0$ ) to make the normalization procedures identical.

Done - see revised version of the figures. This was also relevant to Figs. 7 and 8. Note that the differences in the divergence field in Fig. 7 compared to the previous manuscript version is the result of this change.

15) Page 14, line 14: correct 'the fact that all ...'

Fixed - thank you

16) Page 15: The new spatial convergence study is helpful, but the way it was conducted is questionable. In order to test spatial convergence, one typically selects the smallest time step (to minimize time step errors) and keeps this time step constant. Instead, the authors used the longest time step, kept it constant for decreasing grid spacings and of course observed numerical instabilities at some point. The time step errors could potentially be very large for the shortest grid spacings, and these errors become part of the spatial convergence assessment. I suggest repeating the convergence study and using a very small time step for all simulations to avoid this problem.

What do you mean the longest time step? It is not true that we took a time step for which the greatest grid spacing (lowest resolution) converges, held it fixed and decreased the grid spacing (increased the resolution). We did the opposite, we took the time step for which the results for the finest grid spacing in the previous sections converged and increased the grid spacing (lowered the resolution). Note that all the results of the previous sections, including both the finite difference model and the spectral one, were generated using the same time step of  $\Delta t = 600$  sec used for the convergence analysis in Fig. 10 and using the finest grid spacing in this figure  $\Delta = 0.5^\circ$ . Also how small is very small? In an attempt to address this comment we have repeated the convergence test using a time step of 100 sec (six times smaller) and replaced the results in the Figure, with the new ones. The results remained visually unchanged, but we were able to increase the resolution by another  $0.25^\circ$  and add another data point to the figure. We hope the chosen time step is small enough. We also added a comment on the issue - see revised Section 4.4.

### **Detailed response to the technical issues made by the editor**

#### **Editor P1 Deployability:**

Individual source files in a paper supplement are not particularly easy for language users to employ. This is unfortunate because Python and Matlab (though not really Fortran) provide straightforward mechanisms for packaging files to make them easily installable and usable. In the case of Python, if the package files are then hosted on an online revision control system such as GitHub then users will be able to directly pip install them with a single command. Instructions on how to create a Python package are at <https://packaging.python.org/tutorials/packaging-projects/> while Matlab toolboxes are at: [http://www.mathworks.com/help/matlab/matlab\\_prog/create-and-share-custom-matlab-toolboxes.html](http://www.mathworks.com/help/matlab/matlab_prog/create-and-share-custom-matlab-toolboxes.html).

**Reply:** We agree with the editor on this important point. Thus, the Python code was packaged using PyPi service (<https://pypi.org/>) with the name `pymaws` (PYthon Matsuno Analytical Wave Solutions) and is now fully deployable using the command `pip install pymaws`.

#### **Editor P2 Verification and unit testing:**

There is currently no testing of the code provided. There is little more frustrating when using a test case than to eventually discover that the bug was actually in the test case. Potential users will therefore want to see that there is a robust set of verification tests that demonstrate that the implementation is correct. In this case you have two routes which can both be used.

The first is to check the output of your routines for parameter values where the output is easy to verify. The second is to cross-verify your code by calling all the implementations and checking that their output is the same. For this purpose, it is useful to note that the Matlab code might be callable from Python using <https://pypi.org/project/oct2py/>. It is possible to directly call Fortran from Python using `f2py`, or you could use the Fortran standard C interoperability features to present a public C interface (which would also be a nice user feature!) and call that using `ctypes`. There is some documentation on how to do this in the <https://docs.scipy.org/doc/numpy-1.15.4/user/c-info.python-as-glue.html>. You should use one or more test frameworks (maybe one, maybe you need one for each language) to run the testing in a way that users will understand and which is easy for them to integrate into their own testing frameworks. For example you might use <https://pytest.readthedocs.io/en/latest/>. There are likewise suitable testing frameworks available for Matlab and Fortran (or, if you set up cross-verification, you could just use the Python framework for all languages).

**Reply:** The new code has been thoroughly tested with Python's native `unittest` module. After the installation, the users can run `python test_pymaws.py` in order to verify the code works. Furthermore, all the test procedures are fully documented (i.e., with docstrings), so the users can inspect the test code and integrate it into their own testing frameworks.

### **Editor P3 Code interfaces and naming:**

As far as I can see, the public interface of the code consists primarily of the function `get_fields`, which seems reasonable given that the purpose of the code is to execute one particular test case. However there are a number of things about this interface which are unhelpful. First, the name `get_fields` is problematic. It's not going to be obvious to the user that that is the main function and even what it does. A more descriptive name would be useful, potentially without the `get_` prefix, which adds no information. In Python, the auxiliary routines which are not supposed to be visible outside the package should be prefixed with underscore to mark them as private. In both Matlab and Python, the documentation for functions should be placed in the docstring at the start of the function, not at the start of the file. This change will enable the self-documentation features of these languages to work. It should also be borne in mind that users may see the code without the paper, so it would be a good idea if the docstrings referred back to the paper. The code returns values on a regular latitude-longitude grid. This is not useful for many users. Even many structured grid models have curvilinear grids which are not axis-aligned, and this is before considering unstructured mesh models. The functions should instead evaluate the results at an arbitrary set of latitude-longitude points. The modest performance gain that may be available from the current structure is not worth the cost of having code that many users simply will not be able to use. It is quite conceivable that the user will want to change  $g$ ,  $\Omega$ ,  $A$ , or  $H0$  in order to run the test case for a model using scaled parameters. Currently in Fortran these are private, and in all languages this change would involve changing the global state of the module, which is an unsafe programming practice. It would be better if these parameters were optional arguments to the main function(s), with default values being those given currently. The test case is only valid for certain values of input parameters. In addition to documenting these limitations, the code should check for illegal values and raise appropriate exceptions or return some error, depending on language.

**Reply:** The main function was renamed to `eval_field` for more functional clarity. Furthermore, each function now is fully documented (i.e., with docstrings) and all the private functions were renamed with an underscore preceding their name, as in Python convention. As suggested by the editor, the new code's main function (`eval_field`) now evaluates the results at an arbitrary latitude-longitude point. The users can then call this function on each of their grid points, regardless of its structure. Moreover, the new code supports different input planetary parameters using a global dictionary named `Earth` (default parameters) which can be easily modified per user input. Finally, the new code's functions support raising exceptions for non-appropriate/not-supported user input. For example, the current version of the code supports  $n, k \geq 1$ , so using an input of  $n = 0$  will result in an error message.

#### **Editor P4 License:**

There is currently no license provided with the code. This might mean that the code falls under the same Creative Commons attribution license as the paper, but since the code may be separated from the paper when used, it would be preferable to provide an explicit license. Many authors would use the MIT License in this context, which basically says that users can do anything they like so long as they continue to acknowledge the authorship of the code. See <https://opensource.org/licenses/MIT>. In any event, an explicit license should be chosen and included with the source files.

**Reply:** The new code is now licensed under the MIT open-source license (<https://opensource.org/licenses/MIT>).

#### **Editor P5 GitHub and archiving:**

The steps above will result in quite a lot more files in the implementation, along with a nontrivial directory structure. This could be attached in the supplement, but this has a number of disadvantages. First, there is no mechanism for future bug fixes. Next, direct access mechanisms such as Python's package installer pip will not see the supplement. Instead, the code could be posted on GitHub, which would fix the update and pip problems. GitHub is not a suitable archive location for the canonical version of the code in a manuscript, but GitHub and Zenodo together provide a straightforward way of archiving the repository with a DOI for inclusion in the manuscript. The instructions are at <https://guides.github.com/activities/citable-code/>. GitHub + Zenodo would be a better alternative to the supplement.

**Reply:** Following the editor's suggestion the new code is now posted at GitHub.com (<https://github.com/ofershamir/matsuno>) and its documentation( `README.md` ) includes:

- Installation
- Testing
- Importing
- Example
- Caveats



Furthermore, the documentation demonstrates how to alter the planetary parameters if the user wishes to do so. Finally, as suggested by the editor, the new code release is now archived with Zenodo and can be cited using the DOI:10.5281/zenodo.2605203 (<https://zenodo.org/record/2605203>).

# The Matsuno baroclinic wave test case

Ofer Shamir<sup>1</sup>, Itamar Yacoby<sup>1</sup>, Shlomi Ziskin Ziv<sup>1</sup>, and Nathan Paldor<sup>1</sup>

<sup>1</sup>Fredy and Nadine Herrmann Institute of Earth Sciences, Edmond J. Safra Campus, Givat Ram, The Hebrew University of Jerusalem, Jerusalem, Israel

**Correspondence:** Nathan Paldor (nathan.paldor@huji.ac.il)

**Abstract.** The analytic wave-solutions obtained by Matsuno (1966) in his seminal work on equatorial waves provide a simple and informative way of assessing [the performance of](#) atmospheric models by measuring the accuracy with which they simulate these waves. These solutions approximate the solutions of the shallow water equations on the sphere for small speeds of gravity waves such as those of the baroclinic modes in the atmosphere. This is in contrast to the solutions of the non-divergent barotropic vorticity equation, used in the Rossby-Haurwitz test case, which are only accurate for large speeds of gravity waves such as those of the barotropic mode. The proposed test case assigns specific values to the wave-parameters (gravity wave speed, zonal wave-number, meridional wave-mode and wave-amplitude) for both planetary and inertia gravity waves, and suggests simple assessment criteria suitable for zonally propagating wave solutions. The test is successfully applied to ~~both an equatorial channel~~ a spherical shallow water model ~~, and in an equatorial channel~~ and to a global-scale ~~one~~model. By adding a small perturbation to the initial fields it is demonstrated that the chosen initial waves remain stable for at least 100 wave-periods. The proposed test case can also be used as a resolution convergence test.

*Copyright statement.* TEXT

## 1 Introduction

A cornerstone of global-scale model assessment is the Rossby-Haurwitz test case, originally used by Phillips (1959) as a qualitative way of assessing his shallow water model. Phillips initialized his model with an analytic wave-solution of the non-divergent barotropic vorticity equation obtained by Haurwitz (1940), and examined the spatio-temporal smoothness of the simulated fields at later times. Using this procedure he concluded that the emergent noise in his model was due to a small-but-significant, divergence field missing from the initial fields. Even though the solutions of the non-divergent barotropic vorticity equation are not solution of the Shallow Water Equations (SWEs), Phillips' procedure was adopted by Williamson et al. (1992) as a standard test case for shallow water models and has been extensively used ever since (Jablonowski et al., 2009; Mohammadian and Marshall, 2010; Bosler et al., 2014; Ullrich, 2014; Li et al., 2015, are only five recent examples).

However, there are two known issues with the original Rossby-Haurwitz test case that limit its usefulness (Thuburn and Li, 2000). The first is the generation of small-scale features via potential enstrophy cascade, which requires adequate dissipation mechanisms to remove enstrophy at the grid scale (in order to mimic a continuous cascade to sub-grid scales). The second is

the instability of the initial wave-number 4 used in the Rossby-Haurwitz test case. In contrast to Hoskins (1973) who found that wave-numbers smaller than or equal to 5 are stable, Thuburn and Li show that Rossby-Haurwitz wave-number 4 is in fact also unstable.

5 Recently, Shamir and Paldor (2016) proposed a similar procedure to that of Phillips (1959) where instead of using the solutions of the non-divergent barotropic vorticity equation, the initial fields are the analytic wave-solutions of the linearized SWEs on the sphere derived in Paldor et al. (2013). These solutions fully account for the small divergence field and can be computed on any grid given the locations of the latitudes and longitudes. In particular, they include the fast propagating Inertia-Gravity (IG) waves that are completely absent from the the non-divergent barotropic vorticity equation. Consequently, the procedure proposed by ~~Shamir and Paldor~~ Shamir and Paldor (2016) provides a more quantitative assessment than Phillips's original procedure ~~though~~ while it is just as easy to implement.

Both solutions obtained by Haurwitz (1940) and Paldor et al. (2013) approximate the solutions of the SWEs in the asymptotic limit of large speed of gravity waves. For most practical purposes they are sufficiently accurate for speeds of gravity waves of about  $200 - 300 \text{ ms}^{-1}$  or higher, which are typical of the barotropic mode in Earth's atmosphere and oceans. However, typical speeds of gravity waves of baroclinic modes in the (tropical) atmosphere are about  $20 - 30 \text{ ms}^{-1}$  (Wheeler and Kiladis, 1999). Thus, the above procedures are only relevant for assessing the accuracy with which the barotropic wave mode is simulated. In order to assess the accuracy of the baroclinic wave modes we propose, in the present work, to use the analytic wave-solutions of the linearized SWEs on the equatorial  $\beta$ -plane obtained by Matsuno (1966) that approximate the solutions of the SWEs on the sphere in the asymptotic limit of small speed of gravity waves (De-Leon and Paldor, 2011; Garfinkel et al., 2017).

20 In addition to being on two opposite ends of the spectrum of gravity wave speed the solutions obtained by Matsuno (1966) differ from those obtained by both Haurwitz (1940) and Paldor et al. (2013) in their meridional extent. While the former become negligibly small outside a narrow equatorial band the latter two have non-negligible amplitudes in the vicinity of the poles. Thus, while the Rossby-Haurwitz test case is only relevant to global-scale models, the test case proposed in the present study is applicable to both global-scale and tropical models.

25 A homonymous, but unrelated, test case is the baroclinic wave test case developed in Jablonowski (2004) and Jablonowski and Williamson (2006) and independently in Polvani et al. (2004), and its variants in Lauritzen et al. (2010) and Ullrich et al. (2014). This test case is concerned with the non-linear generation of synoptic-scale eddies in multi-layer models via baroclinic instability. In contrast, the test case proposed here is concerned with linear wave propagation in (non-linear) single-layer models. In particular, while the term baroclinic usually implies the use of multi-layer models, here this term is used to denote single-a single thin layer model of homogeneous density where the gravity waves speeds are similar to those observed in baroclinic modes in the atmosphere.

The idea of using Matsuno's solutions as a test case in a similar fashion to that of the Rossby-Haurwitz test case is most likely not original, but has never been standardized. Thus, the purpose of the present work is to standardize the Matsuno test case in the same spirit that Williamson et al. (1992) standardized the Rossby-Haurwitz one. We start with a short description of the analytic expressions derived by Matsuno (1966) in section 2. The proposed test procedure, including the choice of wave-parameters and assessment criteria, is described in Section 3. In section 4 we demonstrate the usefulness of the proposed

test case using both an equatorial channel spherical shallow water model, and a global-scale one. In addition, we examine the smoothness and stability of the initial waves in a similar fashion to that used in Thuburn and Li (2000) and demonstrate the possibility of using the proposed test case as a resolution convergence test. The paper ends with some concluding remarks in section 5.

## 2 The analytic solutions

The proposed test case is based on the analytic solutions of the SWEs on the equatorial  $\beta$ -plane obtained by Matsuno (1966). These solutions have the form of zonally propagating waves, i.e.

$$\begin{bmatrix} u(x, y, t) \\ v(x, y, t) \\ \Phi(x, y, t) \end{bmatrix} = \text{Re} \left\{ \begin{bmatrix} \hat{u}(y) \\ \hat{v}(y) \\ \hat{\Phi}(y) \end{bmatrix} e^{i(kx - \omega t)} \right\} \quad (1)$$

where  $x$  and  $y$  are the local Cartesian coordinates in the zonal and meridional directions, respectively;  $t$  is time;  $u$  and  $v$  are the velocity components in the zonal and meridional directions, respectively;  $\Phi$  is the geopotential height;  $k$  is the planar zonal wave-number (which has dimensions of  $\text{m}^{-1}$ );  $\omega$  is the wave-frequency; and  $\hat{u}(y)$ ,  $\hat{v}(y)$  and  $\hat{\Phi}(y)$  are the latitude dependent amplitudes; and  $i = \sqrt{-1}$  is the imaginary unit. In accordance with the sign convention used in Matsuno we assume  $k$  is non-negative and let  $\omega$  take any real value. Note, however, that the sign in front of  $\omega$  in (1) is opposite to that in Matsuno's theory. The convention chosen here is more intuitive as it implies that positive values of  $\omega$  correspond to waves that propagate in the positive  $x$  direction, i.e. eastward.

The unknown wave-frequencies and latitude dependent amplitudes are derived from the (well-known) energies and eigenfunctions of the (time-independent) Schrödinger equation of quantum harmonic oscillator. The resulting frequencies are given by the solutions of the following cubic equation

$$\omega_{n,k}^3 - \left[ gHk^2 + \frac{2\Omega\sqrt{gH}}{a}(2n+1) \right] \omega_{n,k} - \frac{2\Omega gHk}{a} = 0, \quad (2)$$

for  $n = -1, 0, 1, 2, \dots$ , where  $\Omega$ ,  $a$  and  $g$  are  $\Omega = 7.29212 \cdot 10^{-5} \text{ rad s}^{-1}$ ,  $a = 6.37122 \cdot 10^6 \text{ m}$  and  $g = 9.80616 \text{ m s}^{-2}$  are the Earth's angular frequency, mean radius, and gravitational acceleration respectively; and  $H$  is the mean layer's depth (thickness).

For  $n \geq 1$  Equation (2) has three distinct real roots corresponding to a slowly westward propagating Rossby wave, a fast Eastward propagating Inertia Gravity (EIG) wave, and a fast Westward propagating Inertia Gravity (WIG) wave. For  $n = 0$  one of the three roots, the one corresponding to a westward propagating gravity wave with  $\omega = -\sqrt{gH}k$ , leads to infinite zonal wind and is thus discarded as a physically reasonable solution. The remaining two roots correspond to the lowest (i.e.  $n = 0$ ) EIG wave and the Mixed Rossby-Gravity (MRG) wave. For  $n = -1$  Equation (2) has one real root  $\omega = \sqrt{gH}k$ , which correspond to the equatorial Kelvin wave (see Matsuno, 1966). The existence of the latter two waves on a sphere is discussed in Garfinkel et al. (2017) and Paldor et al. (2018)

For given values of the zonal wave-number,  $k$ , and meridional mode-number,  $n$ , the roots of the cubic equation can be obtained in a closed analytic form using the solutions of the general cubic equation as follows (e.g. Abramowitz and Stegun,

1964):

$$\omega_{n,k,j} = \text{Re} \left\{ -\frac{1}{3} \left( \Delta_j + \frac{\Delta_0}{\Delta_j} \right) \right\}, \quad \text{for } j = 1, 2, 3 \quad (3)$$

where  $j$  stands for the three roots, and where

$$\Delta_0 = 3 \left[ gHk^2 + \frac{2\Omega\sqrt{gH}}{a}(2n+1) \right], \quad (4a)$$

$$10 \quad \Delta_j = \left[ \frac{\Delta_4 + \sqrt{\Delta_4^2 - 4\Delta_0^3}}{2} \right]^{1/3} \exp\left(\frac{2\pi j}{3}i\right), \quad (4b)$$

$$\Delta_4 = -\frac{54\Omega gHk}{a}. \quad (4c)$$

Given the definitions in (4), the explicit expressions for the frequencies of the Rossby, WIG and EIG waves are obtained by sorting the values in (3) as follows:

$$\text{Rossby :} \quad \omega_{n,k,R} = -\min_{j=1,2,3} |\omega_{n,k,j}|, \quad (5a)$$

$$15 \quad \text{Westward Inertia-Gravity :} \quad \omega_{n,k,WIG} = \min_{j=1,2,3} \omega_{n,k,j}, \quad (5b)$$

$$\text{Eastward Inertia-Gravity :} \quad \omega_{n,k,EIG} = \max_{j=1,2,3} \omega_{n,k,j}. \quad (5c)$$

Having found (one of) the wave-frequencies for a given combination of  $n$  and  $k$ , the corresponding latitude dependent amplitudes can be written as

$$\hat{v}_n = A \underline{H} \hat{H}_n \left( \epsilon^{1/4} \frac{y}{a} \right) \exp\left(-\frac{1}{2} \underline{\epsilon}^{1/2} \left( \epsilon^{1/4} \frac{y}{a} \right)^2\right) \quad (6a)$$

20

$$\hat{u}_{n,k} = \frac{gH\epsilon^{1/4}}{ia(\omega_{n,k}^2 - gHk^2)} \left[ -\sqrt{\frac{n+1}{2}} \left( \frac{\omega_{n,k}}{\sqrt{gH}} + k \right) \hat{v}_{n+1} - \sqrt{\frac{n}{2}} \left( \frac{\omega_{n,k}}{\sqrt{gH}} - k \right) \hat{v}_{n-1} \right] \quad (6b)$$

$$\hat{\Phi}_{n,k} = \frac{gH\epsilon^{1/4}}{ia(\omega_{n,k}^2 - gHk^2)} \left[ -\sqrt{\frac{n+1}{2}} (\omega_{n,k} + \sqrt{gH}k) \hat{v}_{n+1} + \sqrt{\frac{n}{2}} (\omega_{n,k} - \sqrt{gH}k) \hat{v}_{n-1} \right], \quad (6c)$$

for  $n = 1, 2, 3, \dots$  (the cases  $n = -1, 0$  require special treatment), where  $\epsilon = (2\Omega a)^2/gH$  is Lamb's parameter,  $A$  is an arbitrary amplitude (that has dimensions of  $\text{m s}^{-1}$ ), and  $\hat{H}_n$  are the normalized Hermite polynomials of degree  $n$  defined by the following three-term recurrence relation (Press et al., 2007)

$$\underline{\hat{H}}_{-1}(x) = 0, \quad (7a)$$

$$\underline{\hat{H}}_0(x) = \pi^{-1/4}, \quad (7b)$$

$$5 \quad \underline{\hat{H}}_{n+1}(x) = x \sqrt{\frac{2}{n+1}} \hat{H}_n - \sqrt{\frac{n}{n+1}} \hat{H}_{n-1}. \quad (7c)$$

Note: (i) The chosen normalization for the latitude dependent amplitudes in (6) is different from the one used in Matsuno. We use the above normalization for convenience, as it guarantees that  $\hat{v}$  is independent of both  $k$  or  $\omega$ . (ii) The use of the normalized version of the Hermite polynomials also leads to slightly different pre-factors in front of  $\hat{v}_{n+1}$  and  $\hat{v}_{n-1}$  compared to Matsuno. However, they are generally more ~~stable~~computationally stable. (iii) The outer parentheses in (6a) denote the argument of  $\hat{H}_n$  and the exponential function, and not multiplicative factors. In other words, the independent variable in this equation is  $(\epsilon^{1/4}y/a)$ , and not simply  $y$ .

While the solutions obtained by Matsuno (1966) apply for the equatorial  $\beta$ -plane, the proposed test case is intended for use in spherical models. As is shown in Garfinkel et al. (2017), the SWEs on the equatorial  $\beta$ -plane approximate the SWEs on the sphere to zero-order in powers of  $1/\epsilon^{1/4}$ . Thus, the solutions obtained by Matsuno are only accurate in the asymptotic limit  $\epsilon \rightarrow \infty$ . For the fixed values of Earth's angular frequency and mean radius, this implies that the solutions obtained by Matsuno are only accurate for sufficiently small speeds of gravity waves  $\sqrt{gH}$ .

In practice, in order to use Matsuno's solutions in spherical models, the local Cartesian coordinates  $x$  and  $y$  in the above formulae (1) and (6) have to be replaced by the longitude  $\lambda$  and latitude  $\phi$  of the geographical coordinate system. Recall that the transformation from the Cartesian system to the spherical one is  $(x, y) \rightarrow a(\cos \phi_0 \lambda, \phi)$ , where  $\phi_0$  is the central latitude ~~where-at which~~ the planar approximation is applied. Likewise, the planar wave-number  $k$  in ~~all-of-the~~ formulae (1)-(6) has to be replaced by its spherical counterpart,  $k_s$ , using the transformation  $k \rightarrow k_s/a \cos \phi_0$ . Thus, for the equatorial  $\beta$ -plane where  $\phi_0 = 0$ , the transformation is simply  $(x, y) \rightarrow a(\lambda, \phi)$  and  $k \rightarrow k_s/a$ . In particular, the reader should note that the planar wave-number  $k$  has units of  $m^{-1}$  while the spherical wave-number  $k_s$  is dimensionless.

~~Finally, using the above formulae to calculate the waves' latitude dependent amplitudes requires routines for evaluating the normalized Hermite polynomials on any grid given the locations of the latitudes. This can be done using the Hermite three-term recurrence relation, as in Press et al. (2007).~~

### 3 ~~Proposed~~The proposed test procedure

The general procedure of the proposed test case is similar to the Rossby-Haurwitz one in that the model in question is initialized with velocity and height fields corresponding to a particular wave-solution and the time evolution of that wave is then examined. The initial wave fields in this case are taken from the analytic expressions in Section 2. The specific choice of wave-parameters and assessment criteria in the present work are discussed below, separately. As is often the case, these choices represent compromises between conflicting factors, e.g. adherence to observations vs. adherence to asymptotic validity of the analytic solutions or rigorous testing vs. simplicity. In any case, these choices may be the subject of discourse as deemed appropriate by the community.

#### 3.1 wave-parameters

The wave-parameters consist of the speed of gravity waves,  $\sqrt{gH}$ , the wave-number and wave-mode,  $k$  and  $n$ , the wave-amplitude,  $A$ , and the wave-type. Any given combination of these parameters completely specifies a unique wave using

the expressions in (1)-(6). We consider all other parameters, including the spatio-temporal resolution and the form of diffusion/viscosity terms, to be modeling choices left to the developers. This approach is aimed at testing the models in their modus operandi. However, as noted in Polvani et al. (2004), different choices ~~for~~ of the form of diffusion/viscosity terms correspond to different sets of equations and may not converge to the same solutions.

10 The choice of gravity wave speed  $\sqrt{gH}$  is inspired by the observed speed of gravity waves of the baroclinic modes in the atmosphere. In practice, we keep  $g$  fixed to Earth's gravitational acceleration ~~;~~ and set the speed of gravity waves by letting  $H = 30$  m, which is within the range of observed equivalent depths in the equatorial atmosphere (Wheeler and Kiladis, 1999). As mentioned in section 2, the analytic solutions obtained by Matsuno on the equatorial  $\beta$ -plane are only accurate approximations of the SWEs on the sphere in the asymptotic limit of small speeds of gravity waves. The above value was  
 15 found by trial and error to be sufficiently accurate in the sense that it yields stable solutions for at least 100 wave-periods in the simulations described in Section 4.

In addition to the speed of gravity waves, the accuracy of Matsuno's solutions depends also on the wave-number and wave-mode as well. For a given value of  $\sqrt{gH}$ , these solutions become asymptotically accurate in the limits  ~~$k, n \rightarrow 0$  (but  $k \neq 0, k_s, n \rightarrow 0$  (but  $k_s \neq 0$ ))~~ (De-Leon and Paldor, 2011). ~~In addition, the higher the wave-number or wave-mode are, the greater the~~ Also, the spatial variability and the required spatial resolution ~~are. Both both~~ increase with the wave-number or wave-mode so both of these considerations suggest that reasonable choices for the wave-number and wave-mode consist of small to moderate values. The proposed wave-number and wave-mode are  ~~$k=5, k_s=5$  (i.e.  $k=5/a \text{ m}^{-1}$ )~~ and  $n = 1$ , i.e. within the range of dominant values observed in the equatorial atmosphere (Wheeler and Kiladis, 1999), but other choices may work just as well provided  ~~$k, k_s$~~  and  $n$  are not too large.

25 The proposed test case is based on the solutions of the linear SWEs but is intended to be used in non-linear models. Therefore, the waves-amplitude should be sufficiently small so as to satisfy the linearization condition. The proposed amplitude of  $\hat{v}$  in Equation (6) is  $A = 10^{-5} \text{ m s}^{-1}$ , chosen by trial and error so as to enable stable solutions for at least 100 wave periods in the simulations of Section 4.

In general, there are two qualitatively different wave types, Rossby and IG wave, that differ in the magnitude of their divergence and vorticity fields. The former is more solenoidal (non-divergent), whereas the latter is more irrotational. In order to  
 30 assess the models' performances in these two qualitatively different limits we suggest using one of each. Since Rossby waves are exclusively westward propagating, we choose the EIG wave of the two IG waves as the second one case to cover the two directions of longitudinal direction propagation.

~~The resulting wave-periods  $T$  for the~~ For these chosen values of  $\sqrt{gH}$ ,  $k$  and  $n$  the wave-periods,  $T = \frac{2\pi}{\omega}$ , are  $T = 18.5$  days for the Rossby wave and  $T = 1.9$  days for the EIG wave.

### 3.2 Assessment criteria

For sufficiently small wave-amplitudes we expect the spatio-temporal structure of the simulated solutions to be that of zonally  
 5 propagating waves, i.e.  $q = \hat{q}(\phi) e^{i(k\lambda - \omega t)}$  (where  $q$  stands for any of the dependent variables  $u, v$  or  $\Phi$ ), with frequency and latitude dependent amplitudes corresponding to the initial wave. In this case, it is desirable to assess the accuracy of the zonal

and meridional structures of the waves independently. A fast and simple way of doing so is using Hovmöller diagrams, where the temporal change in any direction is isolated by intersecting the fields along a fixed value of the other direction. This results in the following two diagrams:

10 (i) A time-longitude diagram obtained by intersecting the fields at a certain latitude. The contour lines in the time-longitude plane are the set of points satisfying  $k\lambda - \omega t = \text{const}$  (for some real  $\text{const}$ ). Thus, the expected pattern for this diagram is that of straight lines with slopes that equal the inverse of the wave's phase speed  $k/\omega$ . In order to avoid small fluctuations in the vicinity of latitudinal zero-crossings, we recommend using latitudinal intersects at or near local extrema.

(ii) A latitude-time diagram obtained by intersecting the fields at a certain longitude. For any two wave-fronts with an equal  
 15 phase  $k(\lambda_2 - \lambda_1) = \omega(t_2 - t_1)$ . Thus, holding  $\lambda$  fixed while varying  $t$  from  $t_1$  to  $t_2$  is equivalent to holding  $t$  fixed and varying  $\lambda$  from  $\lambda_1$  to  $\lambda_2 = \lambda_1 + \omega/k(t_2 - t_1)$ . The resulting pattern is similar to that of a latitude-longitude diagram, but provides an estimate of the time evolution at a particular longitude (as opposed to a ~~momentary-snapshot~~ latitude-longitude snapshot at a particular time).

Likewise, for zonally propagating waves it is also desirable to isolate the errors in the phase speed and spatial structure.  
 20 As discussed in Shamir and Paldor (2016), the frequently used spherical  $l_2$  error entangles the two, and is therefore of lesser use for assessing the accuracy ~~of propagating waves simulations~~ with which the model simulates a propagating wave. Thus for a more quantitative assessment we suggest using the relative difference between the Root-Mean-Square of the analytic solution and the simulated solutions, i.e.

$$\frac{\sqrt{I[q^2]} - \sqrt{I[q_a^2]}}{\sqrt{I[q_a^2]}}, \quad (8)$$

25 where the quantities  $q$  and  $q_a$  (which can be vectors) correspond to the simulated and analytic solutions, respectively, and where

$$I[q] = \frac{1}{4\pi} \int_0^{2\pi} \int_{-\pi/2}^{\pi/2} q(\lambda, \phi) \cos \phi d\phi d\lambda. \quad (9)$$

Henceforth we refer to the quantity in (8) as the structure-error since, as opposed to the  $l_2$  error, it is unaffected by phase speed errors (i.e. phase shifts in  $\lambda$ ).

## 5 4 Results

In this section we demonstrate the usefulness of the Matsuno test case by applying the proposed procedure to both an equatorial channel finite-difference model and a global-scale spectral one. We then examine the stability of the selected waves/modes in a similar fashion to that used in Thurnburn and Li (2000) for the wave-number 4 Rossby-Haurwitz wave. Finally, we demonstrate the possibility of using the analytic solutions obtained by Matsuno as a resolution convergence test.



## 10 4.1 Demonstration using an equatorial channel finite-difference model

The model is a spherical version of the Cartesian model used in Gildor et al. (2016), in which the integration forward in time is carried out using the conservation form of the SWEs

$$\frac{\partial U}{\partial t} + \frac{1}{a \cos \phi} \frac{\partial}{\partial \lambda} \left( \frac{U^2}{h} \right) + \frac{1}{a} \frac{\partial}{\partial \phi} \left( \frac{UV}{h} \right) - \frac{2UV \tan \phi}{ah} - 2\Omega \sin \phi V = -\frac{g}{2a \cos \phi} \frac{\partial h^2}{\partial \lambda} \quad (10a)$$

$$15 \quad \frac{\partial V}{\partial t} + \frac{1}{a \cos \phi} \frac{\partial}{\partial \lambda} \left( \frac{UV}{h} \right) + \frac{1}{a} \frac{\partial}{\partial \phi} \left( \frac{V^2}{h} \right) - \frac{(U^2 - V^2) \tan \phi}{ah} + 2\Omega \sin \phi U = -\frac{g}{2a} \frac{\partial h^2}{\partial \phi} \quad (10b)$$

$$\frac{\partial h}{\partial t} + \frac{1}{a \cos \phi} \left[ \frac{\partial U}{\partial \lambda} + \frac{\partial (V \cos \phi)}{\partial \phi} \right] = 0, \quad (10c)$$

where  $U = hu$ ,  $V = hv$  and  $h$  is the total layer thickness. The numerical scheme employs a standard finite difference shallow-water solver in which the time-differencing follows a leapfrog scheme (centre differencing in both time and space). The computations were done on an Arakawa C-grid. The model contains provisions for a temporal Robert-Asselin filter, but the filter's coefficient was set to zero in the simulations of the present section. In addition, the model includes no diffusion/viscosity terms.

The computational domain is  $-180^\circ \leq \lambda \leq 180^\circ$  and  $-30^\circ \leq \phi \leq 30^\circ$ . The boundary conditions are periodicity at the zonal boundaries  $\lambda = \pm 180^\circ$  and vanishing meridional velocity at the channel's boundaries  $\phi = \pm 30^\circ$ . [The corresponding values of  \$h\$  and  \$U\$  at the boundaries are determined by the differential equations.](#) For the chosen wave-parameters the amplitude of the meridional velocity  $\hat{v}$  in (6) has an e-folding latitude of  $11^\circ$ , and its amplitude at  $\phi = \pm 30^\circ$  decays to  $4e - 03$  of its maximal value, so the velocity outside the computational domain can be comfortably neglected. The grid-spacing and time step are  $\Delta\lambda = \Delta\phi = 0.5^\circ$  and  $\Delta t = 600$  seconds, which were found to yield stable solutions for at least 100 wave-periods.

Figure 1 shows the initial (top row)  $u, v, \Phi, \xi, \delta$  fields (where  $\xi$  and  $\delta$  are the relative vorticity and divergence, respectively) of the chosen Rossby wave mode, and the resulting latitude-time (middle row) and time-longitude (bottom row) Hovmöller diagrams of the simulated solution. The initial fields were obtained using the analytic expressions of Section 2 and wave-parameters of Section 3.1. [The simulated solutions were obtained using the above equatorial channel model.](#) The chosen intersects used in the calculation of the Hovmöller diagrams are indicated by white dashed lines superimposed on the initial fields, and are also provided in the Figure's caption. For the sake of legibility the shown time domain in each panel is only the last wave periods of the simulation, i.e.  $99T \leq t \leq 100T$ , where  $T$  is the wave-period. The fields are normalized on their global maximum at  $t = 0$ . Thus, white regions correspond to times at which the simulated solution exceeds the initial wave-amplitude, momentarily. With this in mind, recall that the patterns in the latitude-time diagrams are similar to those of a latitude-longitude diagram, and can therefore be used to compare with the initial fields. In general, the initial wave-structure is preserved and the dominant slope in the time-longitude diagrams corresponds to the analytic slope indicated with dashed white lines (bottom row). There are, however, some noticeable deviations: A slight east-west tilt can be observed in the latitude-time diagrams (middle row), but most egregiously, the divergence field is less regular than the other four. We return to this last point at the

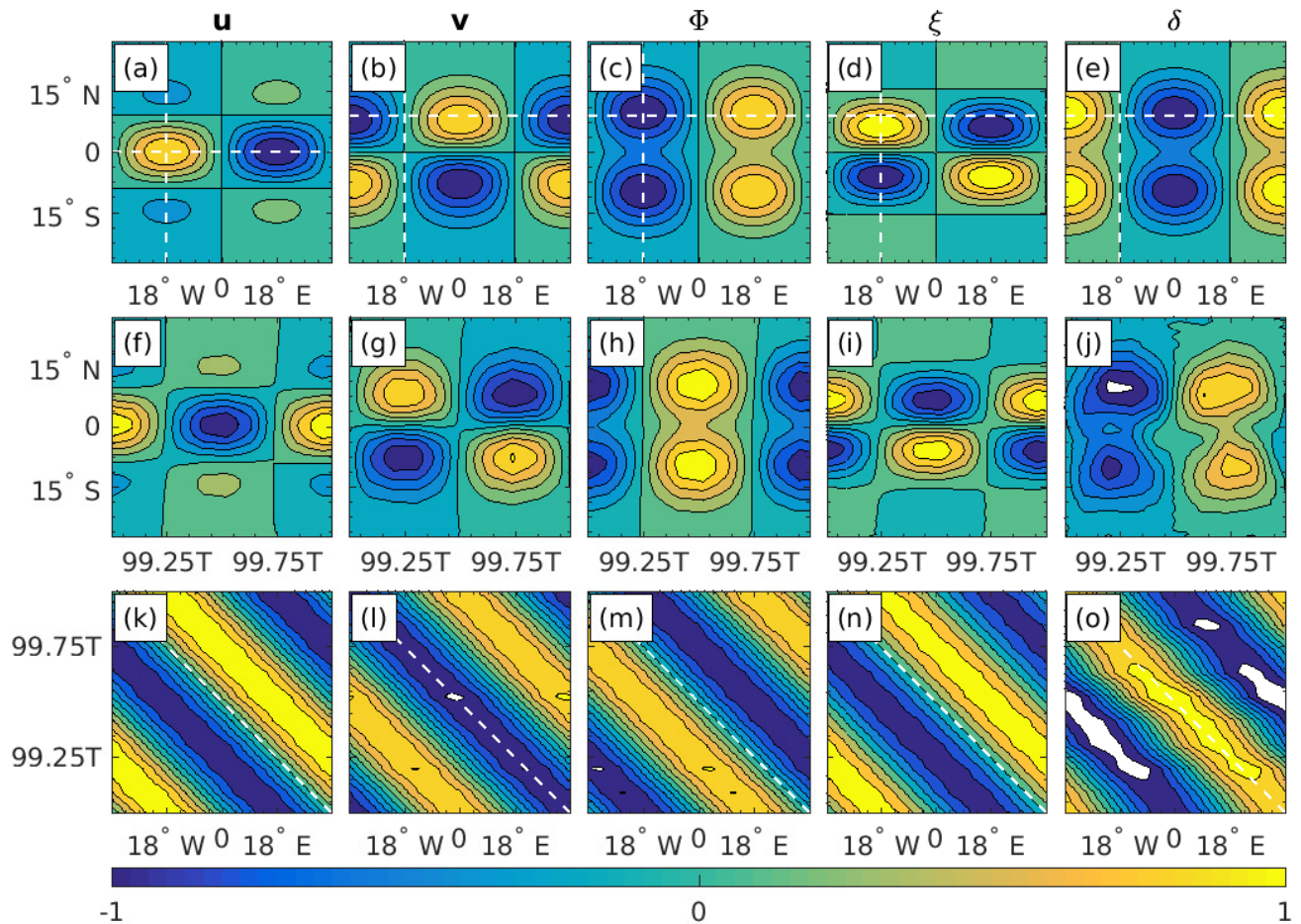


**Figure 1.** Top row: the initial  $u, v, \Phi, \xi, \delta$  Rossby wave fields (top row), obtained using the analytic expressions of Section 2 and wave-parameters of Section 3.1. Middle row: latitude-time Hovmöller diagrams [of the simulated solutions](#), obtained by intersecting the fields at  $\lambda = -18^\circ$  (also indicated by white vertical dashes lines in the top row). Bottom row: [longitude-time time-longitude Hovmöller diagrams of the simulated solutions](#), obtained by intersecting  $u$  at  $\phi = 0^\circ$  and all other fields at  $\phi = 9^\circ$  (also indicated by white horizontal dashes lines in the top row). The [simulated solutions were obtained using the equatorial channel finite difference model](#). The fields are normalized on their global maximum at  $t = 0$ . The wave-period for the chosen wave-parameters is  $T = 18.5$  days. Contour-levels range from  $-1.0$  to  $+1.0$  by  $0.2$ .

5 end of Section 4.3. The [phase of the simulated](#) patterns in the latitude-time diagrams [of the meridional-velocity shown in panel \(g\) is precisely the expected pattern fit the expected patterns](#) considering the westward propagation of the Rossby mode at  $\lambda = -18^\circ$  in one wave-period after [an integer number \(99 in this case\) of](#) wave-periods.

Similarly, Figure 2 shows the initial (top row)  $u, v, \Phi, \xi, \delta$  fields of the chosen EIG wave mode, and the resulting latitude-time (middle row) and time-longitude (bottom row) Hovmöller diagrams of the simulated solution. Note that under the normalization

10 used ~~in the present paper here~~ the initial  $v$  field is independent of the wave type and is therefore identical ~~in both figures. As in~~  
~~to the one in Figure 1. In contrast to~~ Figure 1 the ~~patterns in the latitude-time diagrams of the simulated solutions are noticeably~~  
~~out of phase. However, considering the agreement between the~~ dominant slope in the time-longitude diagrams (~~bottom row~~)  
~~agrees well with the analytic phase speed. In contrast to Figure 1 the latitude-time diagram in panel (g) appears to be  $\pi/4$  out of~~  
~~phase (but can be any integer multiple of  $\pi/4$ ) indicating that in this case there is a small (perhaps even tiny) and the analytic~~  
15 ~~slope indicated by the dashed white lines (bottom row), it is reasonable to say that this phase shift results only from a small~~  
phase speed error that accumulates over time. In addition, in contrast to the Rossby wave in Figure 1, the divergence field in  
this case is just as regular as the other four ~~fields~~.

The structure-error defined in (8) is shown in Figure 3 for both Rossby (top) and EIG (bottom) waves as a function of time.  
In both cases the structure-error fluctuates about a mean value of less than 1% and there is no visible trend throughout the  
20 simulation time of 100 wave-periods. ~~Recall that the structure-error defined in (8) is insensitive to phase differences.~~

## 4.2 Demonstration using a global-scale spectral model

To demonstrate the applicability of the Matsuno wave as a test case for global-scale ~~model-models~~ we use the Geophysical  
Fluid Dynamics Laboratory's (GFDL's) spectral transformed shallow water model which uses the Spherical Harmonics as  
its basis functions (<https://www.gfdl.noaa.gov/idealized-spectral-models-quickstart/>). The chosen spectral resolution was T85,  
25 i.e. a triangular truncation where ~~the highest both the highest retained~~ wave-number and ~~the~~ total wave-number ~~retained both~~  
equal 85. The chosen time step was  $\Delta t = 600$  seconds, as in the equatorial channel model. The model contains provisions for  
hyper-diffusion terms as well as a temporal Robert-Asselin filter, but the coefficients of both were set to zero for the simulations  
described below.

~~Figures 4 and 5 show simulations of the same initial Rossby and EIG waves as in Figures 1 and 2. Figure 4 shows the initial~~  
30 ~~(top row)  $u, v, \Phi, \xi, \delta$  fields (where  $\xi$  and  $\delta$  are the relative vorticity and divergence, respectively) of the chosen Rossby wave~~  
~~mode, and the resulting latitude-time (middle row) and time-longitude (bottom row) Hovmöller diagrams of the simulated~~  
~~solution, obtained using. The initial fields were obtained using the analytic expressions of Section 2 and wave-parameters~~  
~~of Section 3.1. The simulated solutions were obtained using the above GFDL's global-scale spectral model. Note, that unlike~~  
~~Figures 1 and 2, the top row corresponds to the simulated solutions at  $t = 4$  hours, and not~~ The chosen intersects used in the  
calculation of the Hovmöller diagrams are indicated by white dashed lines superimposed on the initial fields, and are also  
provided in the Figure's caption. For the sake of legibility the shown time domain in each panel is only the last wave period of  
the simulation, i.e.  $99T \leq t \leq 100T$ , where  $T$  is the wave-period. The fields are normalized on their global maximum at  $t = 0$ .  
Thus, white regions correspond to times at which the simulated solution exceeds the initial wave-amplitude, momentarily. With  
this in mind, recall that the patterns in the latitude-time diagrams are similar to those of a latitude-longitude diagram, and can  
therefore be used to compare with the initial fields at  $t = 0$ .

~~Unlike the the equatorial channel model, the simulated divergence field. Indeed, the patterns in the latitude-time diagrams~~  
5 ~~of the simulated solutions agree quite accurately with those~~ of the initial ~~Rossby wave in Figure 4 remains as regular as the~~  
~~four other fields~~ wave-structure, but are noticeably out of phase. Nevertheless, considering the agreement between the dominant

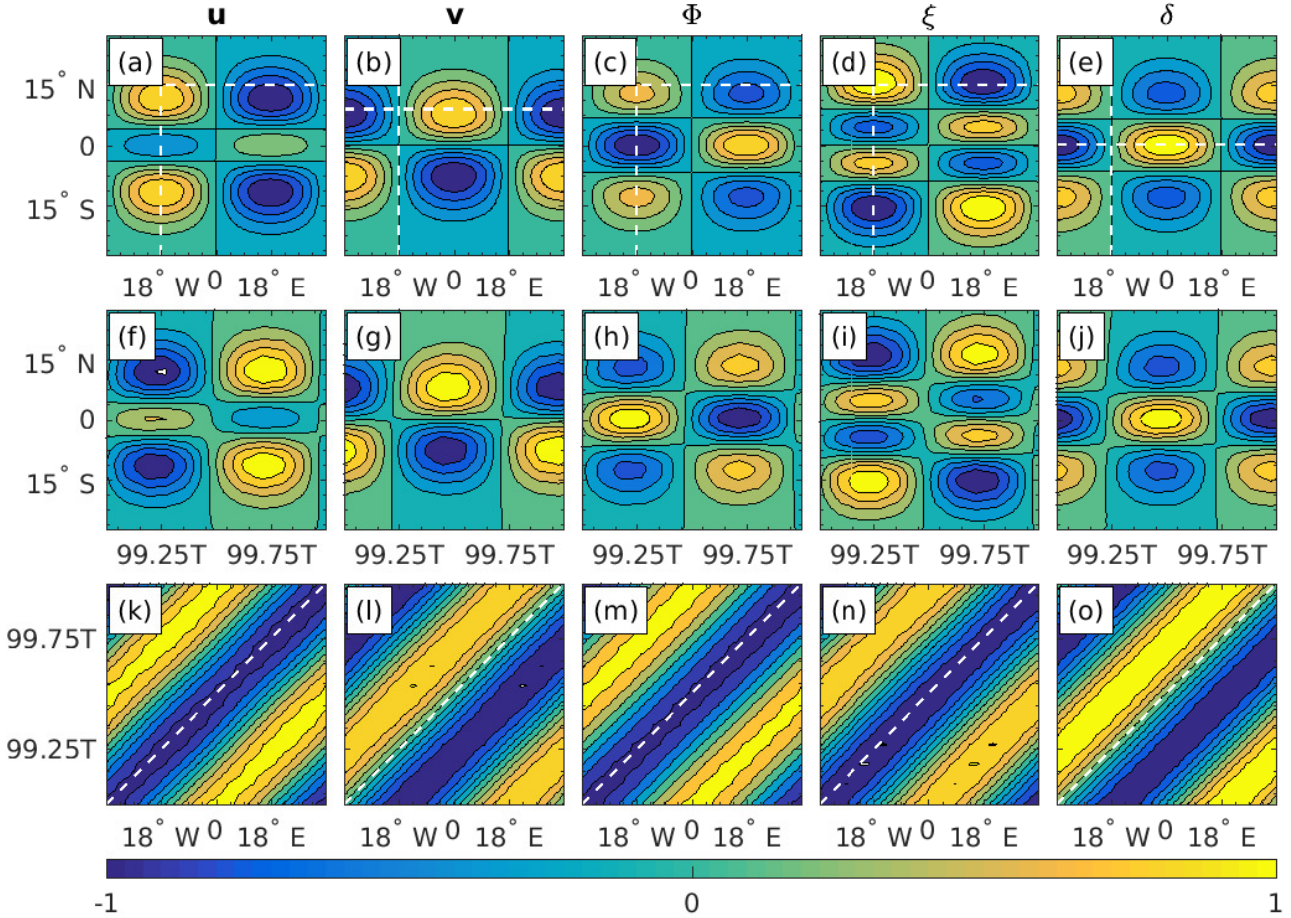


**Figure 2.** Top row: the initial  $u, v, \Phi, \xi, \delta$  EIG wave fields (top row), obtained using the analytic expressions of Section 2 and wave-parameters of Section 3.1. Middle row: latitude-time Hovmöller diagrams of the simulated solutions, obtained by intersecting the fields at  $\lambda = -18^\circ$  (also indicated by white vertical dashes lines in the top row). Bottom row: longitude-time Hovmöller diagrams of the simulated solutions, obtained by intersecting  $v$  at  $\phi = 9^\circ$ ,  $\delta$  at  $\phi = 0^\circ$  and all other fields at  $\phi = 15^\circ$  (also indicated by white horizontal dashes lines in the top row). The simulated solutions were obtained using the equatorial channel finite difference model. The fields are normalized on their global maximum at  $t = 0$ . The wave-period for the chosen wave-parameters is  $T = 1.9$  days. Contour-levels range from  $-1.0$  to  $+1.0$  by  $0.2$ .

slope in the time-longitude diagrams and the analytic slope indicated with dashed white lines (bottom row), it is reasonable to say that this phase shift results from a small phase speed error that accumulates over time. In addition, the divergence field is less regular than the other four fields. We return to this point at the end of Section 4.3. The structure in the-

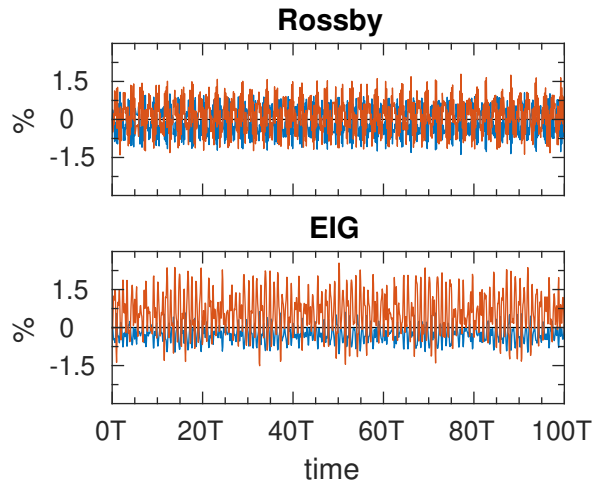


**Figure 3.** The structure-error defined in (8) is shown in Figure 3 for both the Rossby (top) and EIG (bottom) waves as a function of time. Blue: calculated for the velocity vector  $\sqrt{u^2+v^2}\mathbf{u} = (u, v)$ . Red: calculated for the geopotential  $\Phi$ .

10 Similarly, Figure 5 shows the initial (top row)  $u, v, \Phi, \xi, \delta$  fields of the chosen EIG wave mode, and the resulting latitude-time diagrams (middle row) are at slightly out of phase after 99 wave-periods. The simulated EIG wave in Figure 5 is at least  $\pi/4$  and time-longitude (bottom row) Hovmöller diagrams of the simulated solution. Note that under the normalization used in the present paper the initial  $v$  field is independent of the wave type and is therefore identical to the one in Figure 4. As in Figure 4, the patterns in the latitude-time diagrams of the simulated solutions are noticeably out of phase after 99 wave-periods. Finally,

15 but the dominant slope in the time-longitude diagrams (bottom row) agrees well with the analytic slope, indicating that the observed phase shift results from a small phase speed error that accumulates over time.

Finally, the structure-error in Figure 6 is generally similar to the simulations of the equatorial channel model, it fluctuates about a mean value of less than 1% and there are no visible trends throughout the 100 wave-period simulations. Recall that the structure-error defined in (8) is insensitive to phase differences.

### 4.3 Smoothness and stability

In this section we examine the generation of small-scale features and the stability of the proposed wave solutions in a similar fashion to that used in Thuburn and Li (2000) for the original Rossby-Haurwitz wave-number 4.

In Thuburn and Li (2000), the generation of small-scale features and the potential enstrophy cascade is observed by examining the potential vorticity field, which generates tongues that warp-wrap up around themselves and break the initial east-west symmetry. For the small wave-amplitude  $A = 10^{-5} \text{ m s}^{-1}$  used in the present work, the potential vorticity is dominated by the planetary vorticity which is 5-6 orders of magnitudes (depending on the wave) larger than the relative vorticity. Thus, instead of the potential vorticity we examine the relative vorticity (as well as the geopotential). Figures 1-2, as well as Figures 4-5, show the evolution of these two fields between  $t = 99T$  and  $t = 100T$ , where  $T$  is the wave-period in each case. Clearly, both



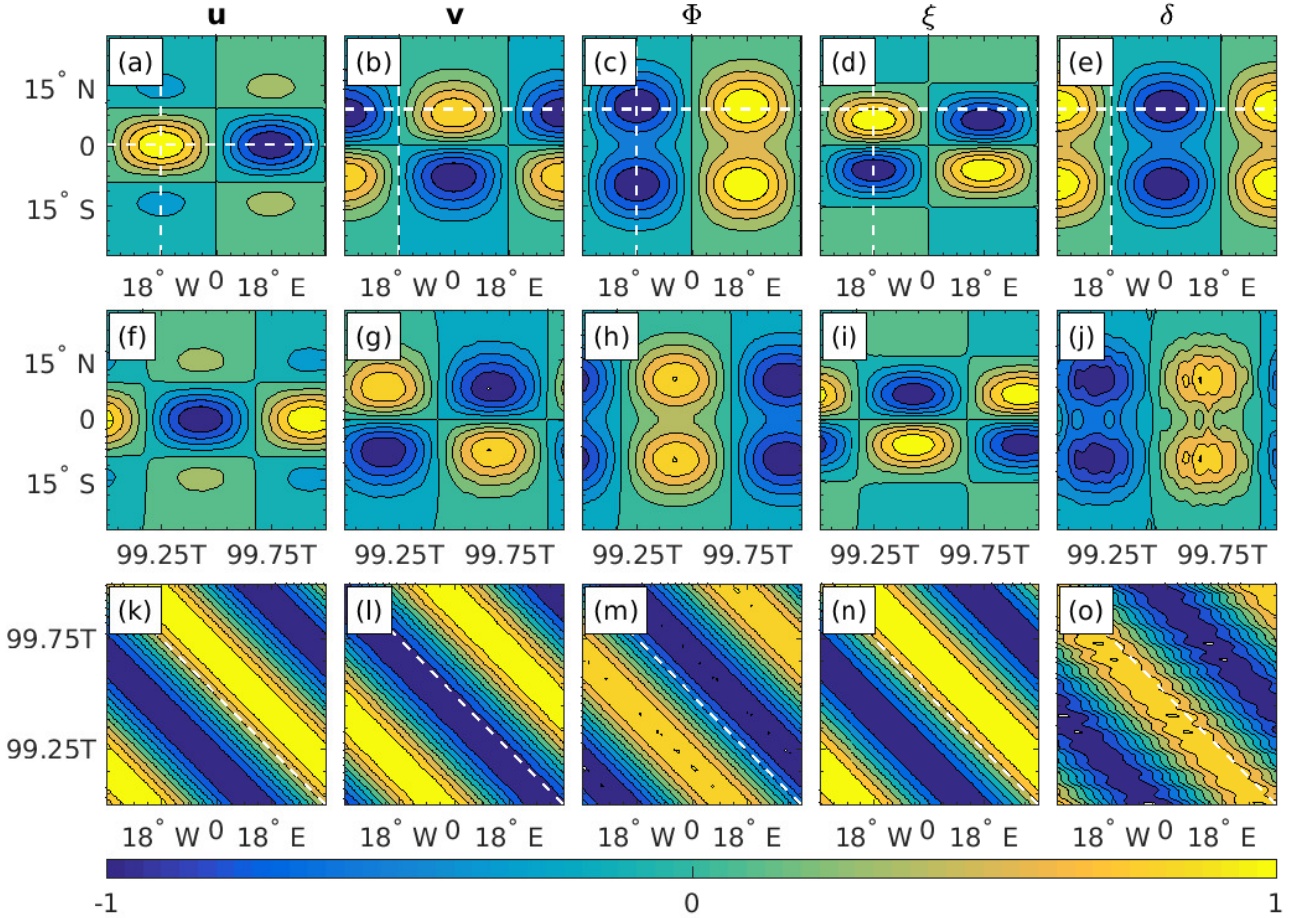


**Figure 4.** Same as Figure 1. Top row: the initial  $u, v, \Phi$ , but  $\xi, \delta$  Rossby wave fields (top row), obtained using GFDL's global-scale spectral model the analytic expressions of Section 2 and wave-parameters of Section 3.1. Note, unlike Figure 1 Middle row: latitude-time Hovmöller diagrams of the simulated solutions, obtained by intersecting the fields at  $\lambda = -18^\circ$  (also indicated by white vertical dashes lines in the top row corresponds to). Bottom row: time-longitude Hovmöller diagrams of the simulated solutions, obtained by intersecting  $u$  at  $t = 4$  hours  $\phi = 0^\circ$  and all other fields at  $\phi = 9^\circ$  (also indicated by white horizontal dashes lines in the top row). The simulated solutions were obtained using GFDL's global-scale spectral model. The fields are normalized on their global maximum at  $t = 0$ . The wave-period for the chosen wave-parameters is  $T = 18.5$  days. Contour-levels range from  $-1.0$  to  $+1.0$  by  $0.2$ .

fields remain regular throughout the simulations and do not develop small-scale features like the ones observed in Thuburn  
 5 and Li (2000). Recall that the simulations in the present work were carried out without any diffusion/viscosity terms. Thus, the  
 simulations remain stable for at least 100 wave-periods with no need to remove potential enstrophy at the grid scale.

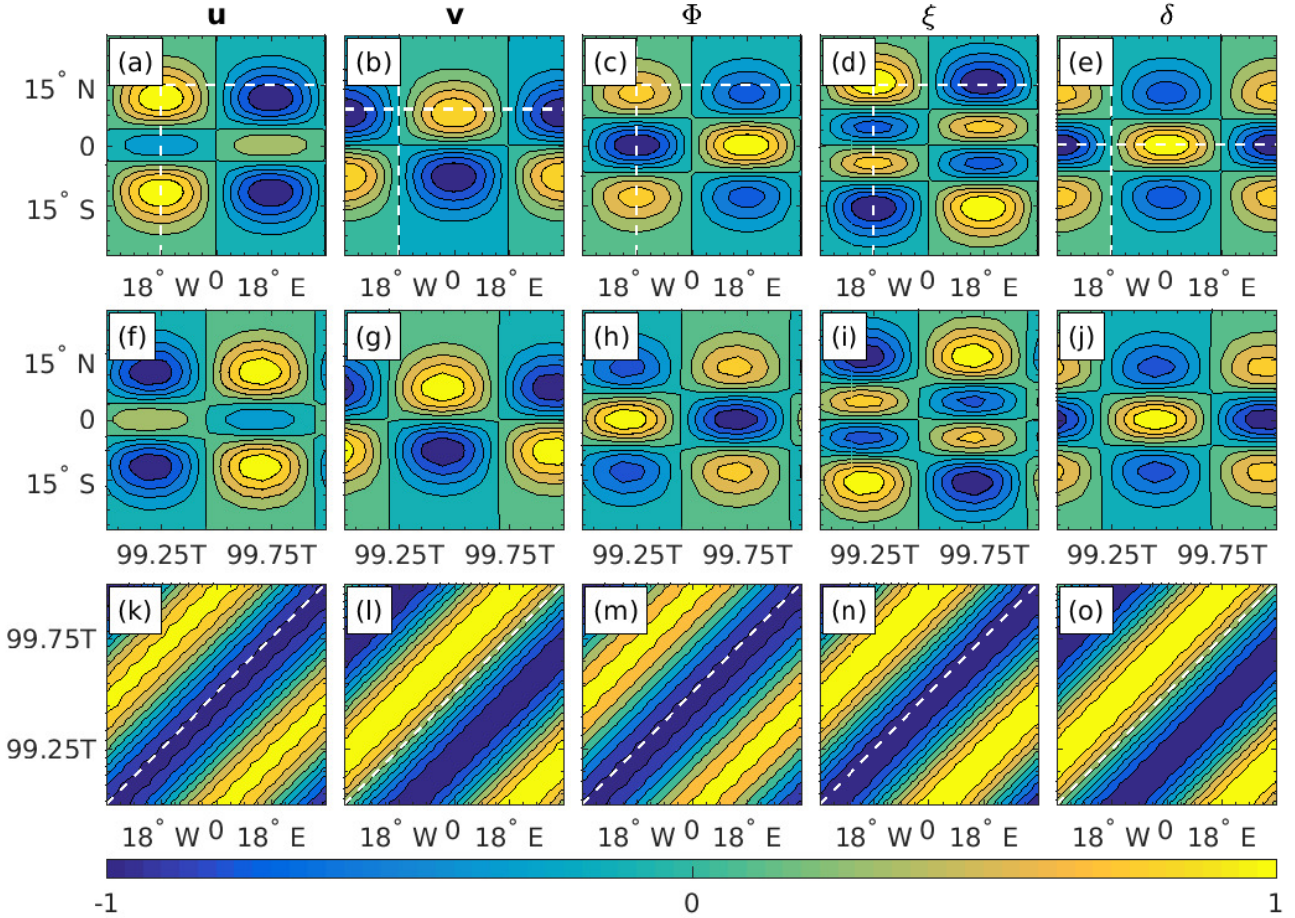


**Figure 5.** Same as Figure 2. Top row: the initial  $u, v, \Phi, \xi, \delta$  EIG wave fields (top row), obtained using GFDL’s global-scale spectral model. Middle row: latitude-time Hovmöller diagrams of the simulated solutions, obtained by intersecting the fields at  $\lambda = -18^\circ$  (also indicated by white vertical dashes lines in the top row). Bottom row: time-longitude Hovmöller diagrams of the simulated solutions, obtained by intersecting  $v$  at  $t = 4$  hours,  $\phi = 9^\circ$ ,  $\delta$  at  $\phi = 0^\circ$  and all other fields at  $\phi = 15^\circ$  (also indicated by white horizontal dashes lines in the top row). The simulated solutions were obtained using GFDL’s global-scale spectral model. The fields are normalized on their global maximum at  $t = 0$ . The wave-period for the chosen wave-parameters is  $T = 1.9$  days. Contour-levels range from  $-1.0$  to  $+1.0$  by  $0.2$ .

In order to examine the stability of the chosen initial waves we repeat the simulations of the previous section with an added perturbation (white noise) to the initial fields. We demonstrate the stability of the waves using only the global-scale model, which was found to yield more stable results when adding the perturbation.

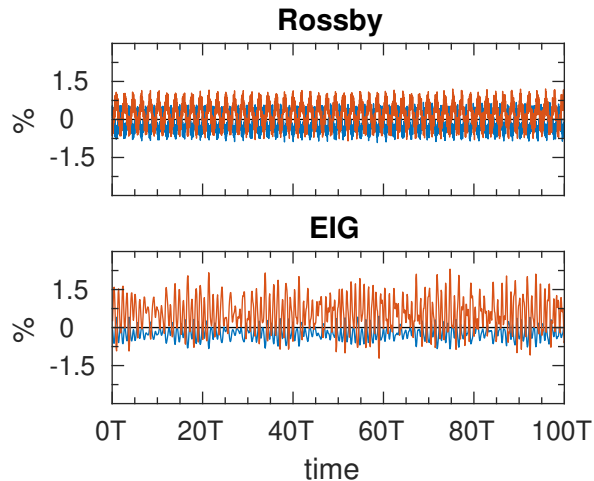


**Figure 6.** Same ~~The structure-error defined in (8) for both the Rossby (top) and EIG (bottom) waves as Figure 3, but using GFDL’s global-scale spectral model~~ a function of time. Blue: calculated for the velocity vector  $\mathbf{u} = (u, v)$ . Red: calculated for the geopotential  $\Phi$ .

10 Figures 7 and 8 show the initial (top) fields of the perturbed Rossby and EIG waves, respectively, ~~at  $t = 4$  hours (top)~~ and the resulting latitude-time (middle row) and time-longitude (bottom row) Hovmöller diagrams of the simulated solution, obtained using GFDL’s global-scale spectral model. The initial perturbation in these figures consist of a uniformly distributed random white noise with amplitude of 5% of the field’s amplitude added to each of the fields  $u, v, \Phi$ . Specifically, let  $q$  stands for any of the variables  $u, v$  or  $\Phi$  then the initial perturbation is given by

$$15 \quad q = q_a + 0.05 \max_{\lambda, \phi} |q_a| (2R - 1), \quad (11)$$

where  $q_a$  is the analytic solutions obtained as in Section 2, and  $R$  is a uniformly sampled random matrix with elements in  $(0, 1)$  whose dimensions are the same as  $q_a$  (in the present work a different  $R$  was drawn for each of the three variables).

Overall, the perturbed waves seem to be stable. The  $u, v$  and  $\Phi$  fields are almost as regular as those of the non-perturbed waves, except for the zero-contour. The small-scale features in the vorticity field of the perturbed Rossby smooth out with time,   
 20 in contrast to the potential vorticity field of the Rossby-Haurwitz wave-number 4. On the other hand, the perturbed Rossby wave divergence field is completely eroded. The vorticity and divergence fields of the perturbed EIG wave are not as regular as those of the non-perturbed wave. However, they ~~do too~~ become smoother with time and the initial wave remains the most dominant wave throughout the entire 100 wave-period simulation. The structure-error in Figure 9 is similar to the previous ones in Figures 3 and 6. These results are quite surprising. We would expect a sufficiently large perturbation to excite other   
 5 modes, regardless of the waves’ stability.

Both the non-perturbed Rossby wave ~~simulated using the equatorial channel model~~ in Sections 4.1 and 4.2, and the perturbed Rossby wave ~~simulated using the global-scale mode of the present section~~ indicate that the divergence field is more sensitive than the other four fields of the Rossby wave. An immediate suspect in this regard is the divergence field amplitude, which is small for the chosen Rossby wave. For reference the meridional wind amplitude for the chosen waves parameters (of both



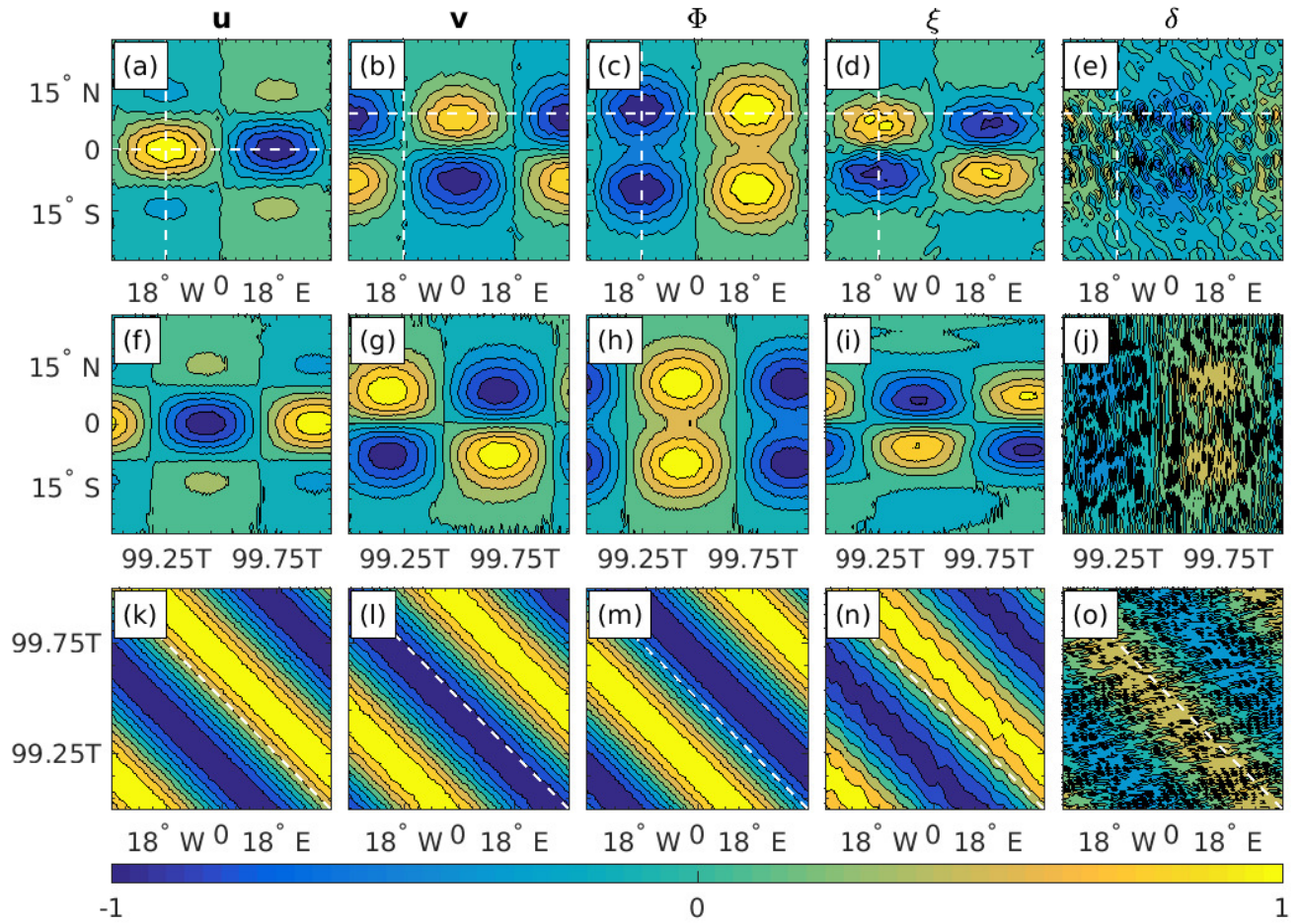


**Figure 7.** Same as Figure 4, but for the perturbed Rossby wave.

the Rossby and EIG waves) is  $6.4e - 6$ , whereas the Rossby wave divergence field amplitude is  $2.6e - 12$ . On the other hand, the divergence field amplitude is only one order of magnitude smaller than the vorticity field amplitude, which is  $2.7e - 11$ . Regardless of the cause, the fact ~~the~~that all other four fields remain quite regular while the divergence field is completely eroded suggests that the small-but-significant divergence field described by Phillips (1959) is in fact a small-and-insignificant one.

#### 4.4 Convergence test for the linear shallow water models

In addition to the test cases proposed by Williamson et al. (1992) a resolution convergence test of linearized SWEs in which the simulations are compared to higher order simulations is also useful for ensuring that the errors decrease with the increase

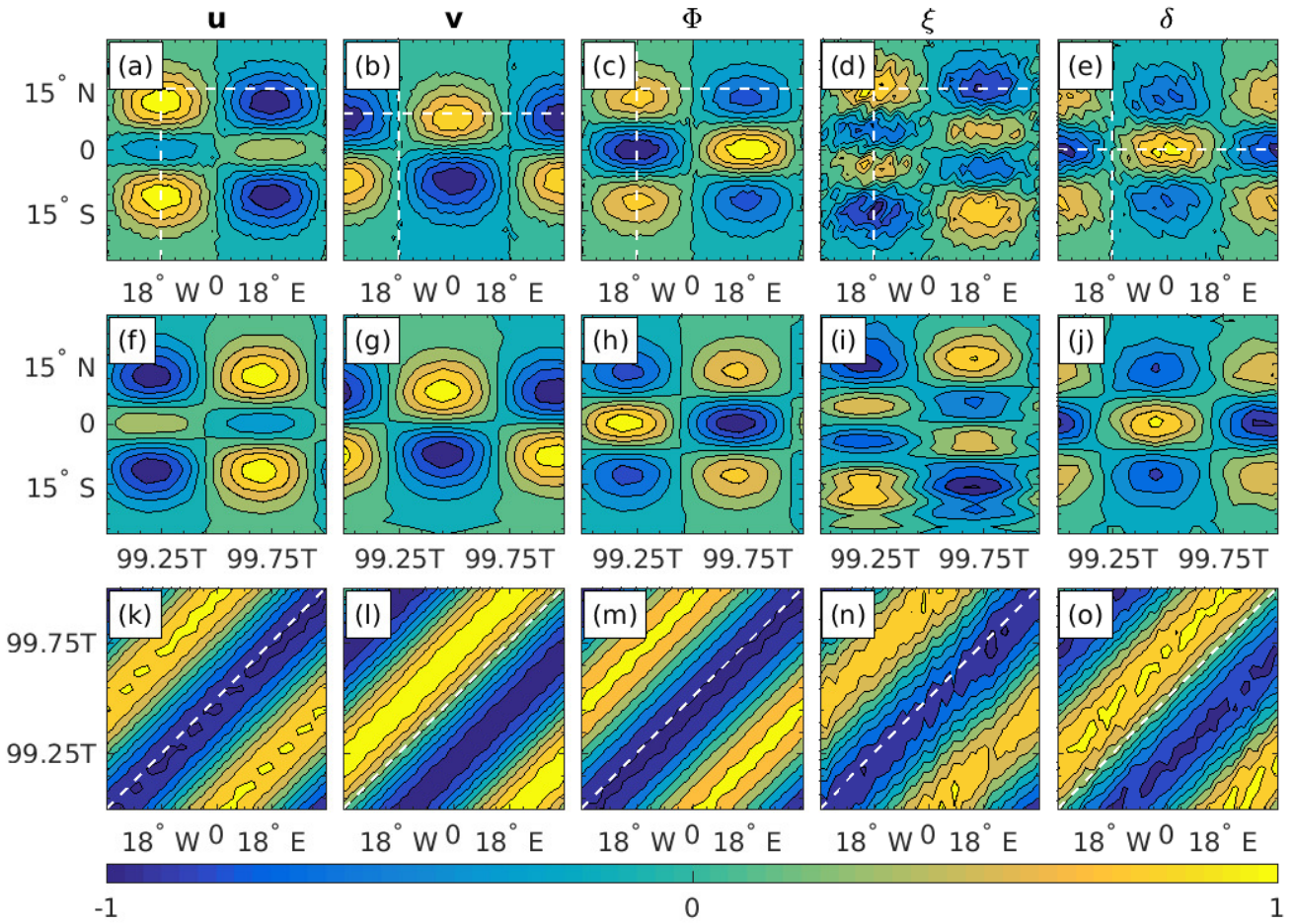


**Figure 8.** Same as Figure 5, but for the perturbed EIG wave.

in resolution. In this section we demonstrate that Matsuno’s analytic wave solutions can be used for this purpose. We use the equatorial channel model which can be easily turned into a linear shallow water model.

Figure 10 shows the structure-error in absolute value as a function of the grid-spacing  $\Delta = \Delta\lambda = \Delta\phi$ , from  $\Delta = 2.5^\circ$  to  $\Delta = 0.5^\circ$  every  $0.25^\circ$ . For each resolution, the initial non-perturbed waves were integrated for 100 wave-periods. As an estimate of the structure-error at each resolution we use the time-series averages (indicated by dots). The error-bars were estimated using the standard deviations of the entire time-series. As the resolution increase from  $\Delta = 2.5^\circ$  to  $\Delta = 0.5^\circ$ , the structure-error time-series average decrease from about about 2% to less than 1%, while the standard deviation decrease from about 2% to about 0.5%. The time step across all resolutions in this figure was held fixed at  $\Delta t = 100$  sec. Note that all the results of the previous sections were obtained for  $\Delta = 0.5^\circ$  and  $\Delta t = 600$  seconds. Attempting to further increase the resolution while holding sec. This time step was found to yield convergent results for  $\Delta = 0.5^\circ$  in the sense that decreasing

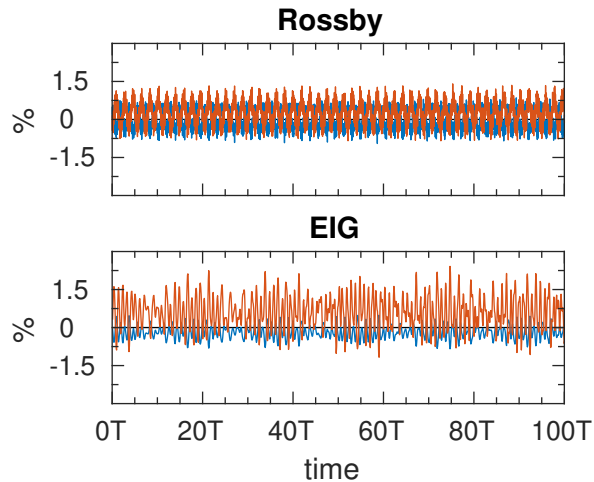


**Figure 9.** Same as Figure 6, but for the perturbed Rossby (top) and EIG (bottom) waves.

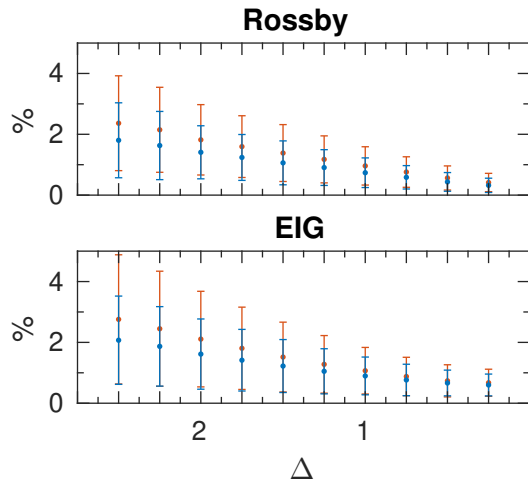


**Figure 10.** Structure-error in absolute value as a function of the grid-spacing  $\Delta = \Delta\lambda = \Delta\phi$ , from  $\Delta = 2.5^\circ$  to  $\Delta = 0.5^\circ$  every  $0.25^\circ$ . The points correspond to the time averaged structure-error over 100 wave-periods, and the error-bars are determined from the standard deviation. Blue: calculated for the velocity vector  $\sqrt{u^2 + v^2} \mathbf{u} = (u, v)$ . Red: calculated for the geopotential  $\Phi$

the time step ~~fixed-cause-the-equatorial-channel-model-to-blow-up, so a smaller time step is required~~ by a factor of two yields no improvements. Nevertheless, for the convergence test of the present section we have further decreased the time step to  $\Delta t = 100$  sec in order to further-improve-the-accuracy allow further increase in the spatial resolution by another  $0.25^\circ$ . This has also enabled a comparison with the results of the previous sections, thus ensuring that the simulations remain stable. Needless to say, for any time step one can expect to encounter numerical instabilities at some (high) spatial resolution.

## 5 Concluding remarks

As vertical resolutions in atmospheric and oceanic models increase it is essential to assess the accuracy with which they resolve baroclinic wave modes, typified by small gravity wave phase speed, in addition to the barotropic mode. To this end we propose to use a similar procedure to that used in the Rossby-Haurwitz test case but ~~replace the~~ with different initial conditions. Instead  
15 of using the analytic solutions obtained by Haurwitz (1940), which are only accurate for large gravity wave speeds such as those of the barotropic mode, we propose to use the analytic solutions obtained by Matsuno (1966), which are accurate for smaller gravity wave speeds such as those of the baroclinic modes.

While Matsuno's solutions apply for the equatorial  $\beta$ -plane, they approximate the solutions of the SWEs on the sphere for the speeds of gravity waves found in the baroclinic modes in the atmosphere, and as demonstrated in the present work  
20 can be accurately simulated in both equatorial channel and global-scale models in spherical coordinates. In addition, unlike the original Rossby-Haurwitz wave-number 4, the chosen initial waves of the present test case remain stable for at least 100 wave-periods, which for the chosen Rossby wave correspond to about 1850 days.

While the solutions of the SWEs obtained by Matsuno (1966) account for the small divergence field missing from the non-divergent Rossby-Haurwitz waves, the results of the present study suggest that this missing divergence field is insignificant.

25 Ideally, we expect the proposed test case to stand on an equal footing alongside the Rossby-Haurwitz one, but in the words of Williamson et al. (1992): "The test will only become standard to the extent that the community finds it useful".

*Code availability.* A Python module for evaluating the initial conditions and analytic solutions is publicly available under the MIT license at <https://github.com/ofershmir/matsuno>, and archived on Zenodo at <http://doi.org/10.5281/zenodo.2605203>.

*Data availability.* TEXT

*Code and data availability.* TEXT

*Sample availability.* TEXT

*Author contributions.* NP conceived the idea of standardizing the Matsuno test case for General Circulation Models in spherical coordinates. IY adopted the Cartesian shallow water model used in Gildor et al. (2016) to spherical coordinates and was responsible for the numerical  
5 simulations. OS analyzed the numerical results, prepared the manuscript and ran the GFDL spectral global model. SZZ prepared the IC generating code for packaging, deployment, testing and licensing.

*Competing interests.* The authors declare that they have no conflict of interest.

*Disclaimer.* TEXT

*Acknowledgements.* H-Z. Krugliak and Dr. C. I. Garfinkel of HU helped us install and run the GFDL model. We also acknowledge the  
10 helpful discussions we had with Dr. Y. De-Leon of HU.

## References

- Abramowitz, M. and Stegun, I. A.: Handbook of Mathematical Functions with Formulas, Graphs, and Mathematical Tables, vol. 56 of *National Bureau of Standards Applied Mathematics Series*, Dover, <https://doi.org/10.1119/1.15378>, 1964.
- Bosler, P., Wang, L., Jablonowski, C., and Krasny, R.: A Lagrangian particle/panel method for the barotropic vorticity equations on a rotating  
15 sphere, *Fluid Dynamics Research*, 46, 031 406, 2014.
- De-Leon, Y. and Paldor, N.: Zonally propagating wave solutions of Laplace Tidal Equations in a baroclinic ocean of an aqua-planet, *Tellus A*, 63, 348–353, <https://doi.org/10.1111/j.1600-0870.2010.00490.x>, 2011.
- Garfinkel, C. I., Fouxon, I., Shamir, O., and Paldor, N.: Classification of eastward propagating waves on the spherical Earth, *Quarterly Journal of the Royal Meteorological Society*, 143, 1554–1564, 2017.
- 20 Gildor, H., Paldor, N., and Ben-Shushan, S.: Numerical simulation of harmonic, and trapped, Rossby waves in a channel on the midlatitude  $\beta$ -plane, *Quarterly Journal of the Royal Meteorological Society*, 142, 2292–2299, 2016.
- Haurwitz, B.: The motions of the atmospheric disturbances on the spherical earth, *J. mar. Res.*, pp. 254–267, 1940.
- Hoskins, B. J.: Stability of the Rossby-Haurwitz wave, *Quarterly Journal of the Royal Meteorological Society*, 99, 723–745, <https://doi.org/10.1002/qj.49709942213>, <https://rmets.onlinelibrary.wiley.com/doi/abs/10.1002/qj.49709942213>, 1973.
- 25 Jablonowski, C.: Adaptive grids in weather and climate modeling, Ph.D. thesis, University of Michigan, Ann Arbor, MI, USA, 2004.
- Jablonowski, C. and Williamson, D. L.: A baroclinic instability test case for atmospheric model dynamical cores, *Quarterly Journal of the Royal Meteorological Society*, 132, 2943–2975, 2006.
- Jablonowski, C., Oehmke, R. C., and Stout, Q. F.: Block-structured adaptive meshes and reduced grids for atmospheric general circulation models, *Philosophical Transactions of the Royal Society of London A: Mathematical, Physical and Engineering Sciences*, 367, 4497–  
30 4522, 2009.
- Lauritzen, P. H., Jablonowski, C., Taylor, M. A., and Nair, R. D.: Rotated versions of the Jablonowski steady-state and baroclinic wave test cases: A dynamical core intercomparison, *Journal of Advances in Modeling Earth Systems*, 2, 2010.
- Li, X., Peng, X., and Li, X.: An improved dynamic core for a non-hydrostatic model system on the Yin-Yang grid, *Advances in Atmospheric Sciences*, 32, 648–658, 2015.
- 35 Matsuno, T.: Quasi-geostrophic motions in the equatorial area, *Journal of the Meteorological Society of Japan. Ser. II*, 44, 25–43, 1966.
- Mohammadian, A. and Marshall, J.: A “vortex in cell” model for quasi-geostrophic, shallow water dynamics on the sphere, *Ocean Modelling*, 32, 132–142, 2010.
- Paldor, N., De-Leon, Y., and Shamir, O.: Planetary (Rossby) waves and inertia–gravity (Poincaré) waves in a barotropic ocean over a sphere, *Journal of Fluid Mechanics*, 726, 123–136, 2013.
- Paldor, N., Fouxon, I., Shamir, O., and Garfinkel, C. I.: The mixed Rossby–gravity wave on the spherical Earth, *Quarterly Journal of the Royal  
5 Meteorological Society*, 144, 1820–1830, <https://doi.org/10.1002/qj.3354>, <https://rmets.onlinelibrary.wiley.com/doi/abs/10.1002/qj.3354>, 2018.
- Phillips, N. A.: Numerical integration of the primitive equations on the hemisphere, *Monthly Weather Review*, 87, 333–345, [https://doi.org/10.1175/1520-0493\(1959\)087<0333:NIOTPE>2.0.CO;2](https://doi.org/10.1175/1520-0493(1959)087<0333:NIOTPE>2.0.CO;2), 1959.
- Polvani, L. M., Scott, R., and Thomas, S.: Numerically converged solutions of the global primitive equations for testing the dynamical core  
10 of atmospheric GCMs, *Monthly weather review*, 132, 2539–2552, 2004.

- Press, W. H., Teukolsky, S. A., Vetterling, W. T., and Flannery, B. P.: Numerical recipes 3rd edition: The art of scientific computing, Cambridge university press, 2007.
- Shamir, O. and Paldor, N.: A quantitative test case for global-scale dynamical cores based on analytic wave solutions of the shallow-water equations, *Quarterly Journal of the Royal Meteorological Society*, 142, 2705–2714, 2016.
- Thuburn, J. and Li, Y.: Numerical simulations of Rossby–Haurwitz waves, *Tellus A*, 52, 181–189, 2000.
- 420 Ullrich, P. A.: A global finite-element shallow-water model supporting continuous and discontinuous elements, *Geoscientific Model Development*, 7, 3017–3035, 2014.
- Ullrich, P. A., Melvin, T., Jablonowski, C., and Staniforth, A.: A proposed baroclinic wave test case for deep-and shallow-atmosphere dynamical cores, *Quarterly Journal of the Royal Meteorological Society*, 140, 1590–1602, 2014.
- Wheeler, M. and Kiladis, G. N.: Convectively coupled equatorial waves: Analysis of clouds and temperature in the wavenumber–frequency  
425 domain, *Journal of the Atmospheric Sciences*, 56, 374–399, 1999.
- Williamson, D. L., Drake, J. B., Hack, J. J., Jakob, R., and Swarztrauber, P. N.: A standard test set for numerical approximations to the shallow water equations in spherical geometry, *Journal of Computational Physics*, 102, 211–224, [https://doi.org/10.1016/S0021-9991\(05\)80016-6](https://doi.org/10.1016/S0021-9991(05)80016-6), 1992.